Precise Subnanometer Plasmonic Junctions for SERS within Gold Nanoparticle Assemblies Using Cucurbit[*n*]uril "Glue"

Richard W. Taylor,[†] Tung-Chun Lee,[‡] Oren A. Scherman,[‡] Ruben Esteban,[§] Javier Aizpurua,[§] Fu Min Huang,[†] Jeremy J. Baumberg,[†] and Sumeet Mahajan[†,*]

[†]NanoPhotonics Centre, Cavendish Laboratory, University of Cambridge, Cambridge CB3 0HE, U.K., [‡]Melville Laboratory for Polymer Synthesis, Department of Chemistry, University of Cambridge, Cambridge CB2 1EW, U.K., and [§]Centro de Física de Materiales, Centro Mixto CSIC-UPV/EHU and Donostia International Physics Center (DIPC), Donostia-San Sebastián, 20018, Spain

ABSTRACT Cucurbit[*n*]urils (CB[*n*]) are macrocyclic host molecules with subnanometer dimensions capable of binding to gold surfaces. Aggregation of gold nanoparticles with CB[*n*] produces a repeatable, fixed, and rigid interparticle separation of 0.9 nm, and thus such assemblies possess distinct and exquisitely sensitive plasmonics. Understanding the plasmonic evolution is key to their use as powerful SERS substrates. Furthermore, this unique spatial control permits fast nanoscale probing of the plasmonics of the aggregates "glued" together by CBs within different kinetic regimes using simultaneous extinction and SERS measurements. The kinetic rates determine the topology of the aggregates including the constituent structural motifs and allow the identification of discrete plasmon modes which are attributed to disordered chains of increasing lengths by theoretical simulations. The CBs directly report the near-field strength of the nanojunctions they create *via* their own SERS, allowing calibration of the enhancement. Owing to the unique barrel-shaped geometry of CB[*n*] and their ability to bind "guest" molecules, the aggregates afford a new type of *in situ* self-calibrated and reliable SERS substrate where molecules can be selectively trapped by the CB[*n*] and exposed to the nanojunction plasmonic field. Using this concept, a powerful molecular-recognition-based SERS assay is demonstrated by selective cucurbit[*n*]uril host–guest complexation.

KEYWORDS: plasmon · cucurbit[*n*]urils · nanoparticle · SERS · hot spot · sensing

The discovery of enormous Raman signals from roughened silver electrodes[1] along with understanding of the electric field enhancement mechanism sparked the promise of powerful surface-enhanced Raman spectroscopies (SERS).[2–7] In particular, SERS enhancements as high as 10^{10}–10^{14} derived from discrete gold nanocolloid assemblies, which amplify the electromagnetic field confined between closely coupled nanopairs, have permitted sensing of single molecules.[8–18] The ability to reproducibly control the interstitial regions of intense field amplification (so-called "hot spots") for reliable detection and identification of single molecules is a much vaunted goal of the SERS research community.

One of the most critical issues for achieving reproducible hot spots is the control of the gap size between plasmonic structures with subnanometer precision. Despite this, most work has concentrated more on the fabrication of the nanoparticles than control of these gaps. Control of the subnanometer critical dimension over large areas to create such hot spots uniformly is nontrivial. Even more difficult is placing analyte molecules precisely within these junctions of ultrahigh field enhancement. The simplest and most studied system for the generation of such hot spots is through aggregation of nanoparticle colloids. Although a huge understanding of colloid aggregates exists due to numerous experimental, theoretical, and computational studies over the past 30 years,[19–26] their widespread adoption as a practical SERS substrate has so-far been hindered by irreproducible performance.[27,28] For example, aggregates formed through the "salting" of citrate-capped colloids tend to display poor control over size, gap, and topology, while organic monolayer-capped assemblies exhibit inconsistent and broad particle spacing[29,30] (Figure 1a); supposedly, "rigid" linking molecules such as DNA, biotin-streptavidin, or multivalent thiols (Figure 1b)[31–35] restrict access to the hot spot they define and have not been rigid in practice (they do not show the features we report here).

Despite this vast amount of work on coagulation aggregates, crucial control over both particle spacing and the placement of molecules in these hot spots while linking the SERS to plasmon modes by simultaneous measurements has not been carried

* Address correspondence to sm735@cam.ac.uk.

Received for review January 20, 2011 and accepted April 13, 2011.

Published online April 13, 2011
10.1021/nn200250v

© 2011 American Chemical Society

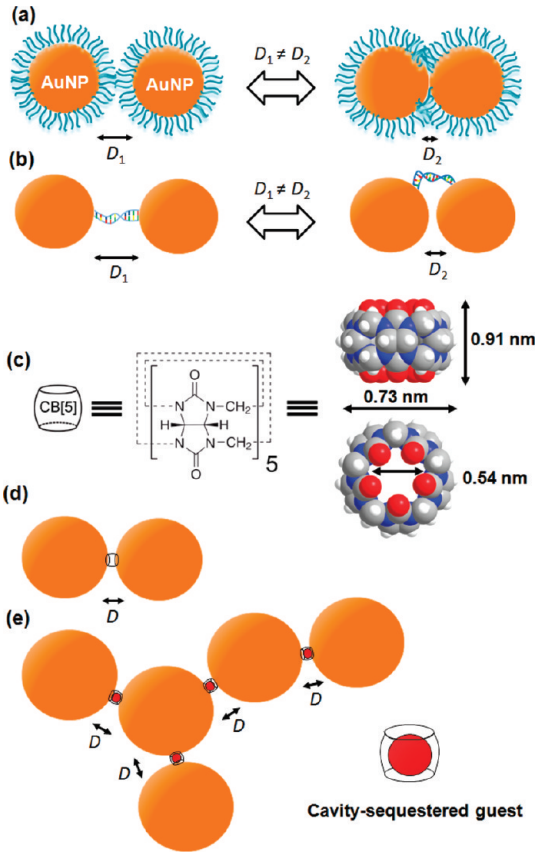

Figure 1. (a,b) Current strategies to generate a coagulate of AuNPs produce inconsistent and uncontrollable interparticle spacing through (a) organic-capped colloids or (b) DNA-mediated linkers. (c) Cucurbit[5]uril composed of five cyclically arranged glycouril units, with a hydrophobic internal cavity and polar carbonyl portals that bind to the Au surface. (d) AuNPs glued into a dimer by CB[*n*] with portal-to-portal separation rigidly fixed at 0.9 nm. No other binding configuration is possible. (e) CB[*n*] cavity supports selective guest sequestration, leading to the use of AuNP:CB[*n*] aggregates for molecular-recognition-based SERS assays where the CB[*n*] defines the nanojunctions.

out. CB[5] is a rigid barrel-shaped molecule (Figure 1c) that binds to the Au surface through the carbonyl groups at the portals[36,37] and thus fixes the separation between gold nanoparticles at a precise 0.9 nm. The portal separation is the same among all CB[*n*]s.[38,39] We demonstrate here the reproducible plasmonics of AuNP:CB[5] aggregates arising due to the fixed interparticle spacing due to binding by CBs. Both CB[5] and CB[7] are water-soluble and Raman-active.[5] Thus CB[*n*] not only acts to define the hot spot junction but also, by being Raman-active, allows local reporting of the field confinement within the center of the junction *via* SERS. Furthermore, the internal cavity common to all cucurbit[*n*]urils is known to form host–guest complexes with a range of hydrophobic guests,[38–40] thus, when incorporated in such nanoaggregates, opens the exciting possibility of positioning the guests in the very center of the intense confined electric field (hot spot) for optimal sensing. Specificity for guest binding can be achieved through selection of a CB[*n*] with an appropriately sized cavity or a guest with compatible chemistry. Such exquisite control over both the creation of numerous exact separations and precise electromagnetic modes, and the positioning of analyte molecules is unprecedented and has not been demonstrated in any other system for SERS.

Although the ability of CB[*n*] to induce conglomeration of AuNPs has been shown,[36,37] crucially neither the *in situ* plasmonic evolution of the aggregates nor their utilization in SERS has been reported. We report the kinetics of plasmonic evolution recorded spectroscopically on the millisecond time scale, which is found to be consistent with known reaction-limited and diffusion-limited colloidal growth (RLCA and DLCA) models.[41–44] The discrete nature of the optical coupling between the NPs in the aggregate allows for a new approach to real-time reporting of local aggregate growth in the far-field. Most importantly, we find that distinct structural entities comprising the aggregates support the different plasmon modes and provide spectral, theoretical, and microscopic evidence for them. We also relate the kinetics of the SERS intensity, reported by the incorporated CBs themselves, to that of the evolving plasmon mode by simultaneous extinction and Raman measurements. This allows us to determine the corresponding near-field properties of the aggregates in time. Furthermore, the well-defined plasmon modes arising due to the precise gap generated by CBs tune into resonance with common Raman excitation wavelengths. In this paper, we report the kinetic evolution of different plasmon modes resulting from CB[5]-mediated assembly of AuNPs, the relationship of the topology of the aggregates and their constituent structural entities to the plasmon modes, which are supported by simulations, and the consequent utilization of CBs as SERS reporters for a self-calibrated *in situ* SERS substrate. Finally, we successfully demonstrate the first utilization of these CB[*n*]-mediated SERS substrates for selective host–guest detection.

RESULTS AND DISCUSSION

The rich host–guest chemistry of cucurbit[*n*]urils along with their rigid geometry and ability to bind to gold makes them a prime candidate for mediating aggregation of nanoparticles to form accessible hot spots for use in SERS. In order to understand the effect of CB[5] on the plasmonics of aggregation, we studied the resulting change in optical extinction, in a time-resolved manner, as a function of CB[5] concentration. This modifies the CB surface coverage on the AuNPs (always here extremely sparse), which determines the likelihood of a collision resulting in coagulation between two CB-capped AuNPs and hence the rate of global aggregation. While the detailed results we report

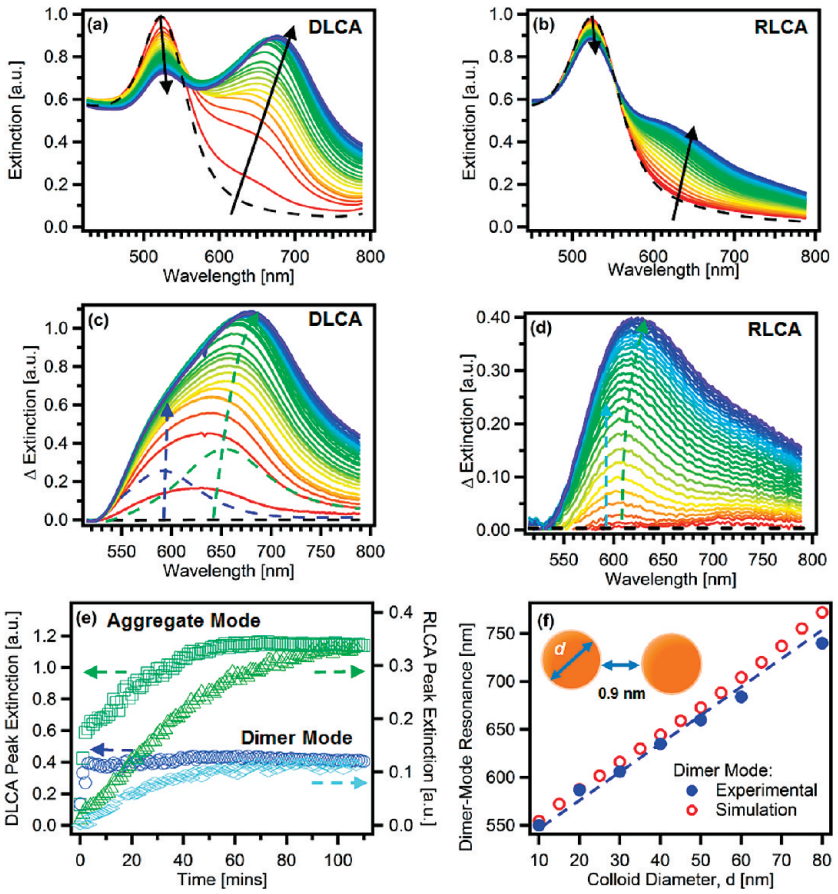

Figure 2. (a,b) Time-resolved extinction spectra of aggregating AuNP:CB[5] samples for (a) DLCA (1:80) and (b) RLCA (1:60) kinetics (arrows guide the eye). Spectra acquired at 1 min intervals for 2 h. (c,d) Difference spectra obtained from (a,b) by removing the isolated single AuNP contributions. Extinction difference fits best to sum of two Lorentzian modes (dashed) which grow with time. (e) Extracted intensity with time of dimer-like mode at 590 nm (blue, light-blue for DLCA, RLCA) and coupled chain mode (green, light-green for DLCA, RLCA). (f) Measured plasmon resonance of CB[5]-coupled dimer-like mode as a function of AuNP diameter, with the theoretical simulations performed using the boundary element method[45] using the dielectric function for Au from Johnson and Christy.[46] Simulations include size corrections and assumes a particle separation of 0.9 nm. The electric field is polarized parallel to the interparticle axis.

here are for 20 nm AuNPs, similar results are seen for diameters from 10 to 100 nm AuNPs.

Time-Resolved Extinction of AuNP:CB[5] Assemblies. Time-resolved UV–vis spectra representative of the two main kinetic growth regimes at AuNP:CB[5] ratios of 1:80 and 1:60 are shown in Figure 2a,b. Higher CB[5] ratios correspond to diffusion-limited growth of the AuNPs since their sticking probability is high and collisions are more likely to result in successful coagulation. For low concentrations of CB[5], the aggregation is reaction-limited as fewer collisions result in aggregation. The submillisecond acquisition of the evolving spectra is continued over 2 h (progressing according to the arrows). Spectral features for both kinetic growth regimes are discussed below. However, it is apparent that the information is rather different from that provided by quasi-static light scattering, which under model assumptions gives the fractal dimension of the aggregates[44] and dynamic light scattering which under further assumptions suggests the cluster anisotropy.[42,43] The spectra instead here reveal the smallest-scale features of the aggregates from the coupling of particles.

Aggregation of the AuNPs in the DLCA regime (Figure 2a) shows extinction spectra which rapidly decrease and broaden the surface plasmon resonance (SPR) band of the AuNP at 525 nm[47,48] as well as the appearance of a strong secondary broad band centered at 650 nm, arising from the aggregation. Over time, this aggregate band red shifts to a maximum of 690 nm. Aggregation proceeding in the RLCA regime (1:60, Figure 2b) over 2 h follows a similar but much slower growth curve corresponding to the first 2 min of the 1:80 AuNP:CB[5] aggregate. Notably, similar plasmonic properties are achieved through different growth routes, which are due to the reproducible nature of the interparticle mediation.

To isolate the 600–700 nm aggregate plasmon band in greater detail, the difference spectra of Figure 2a,b are obtained by subtracting proportionate amounts of the single AuNP spectra to give Figure 2c,d. Decomposition of the broad aggregate band for both

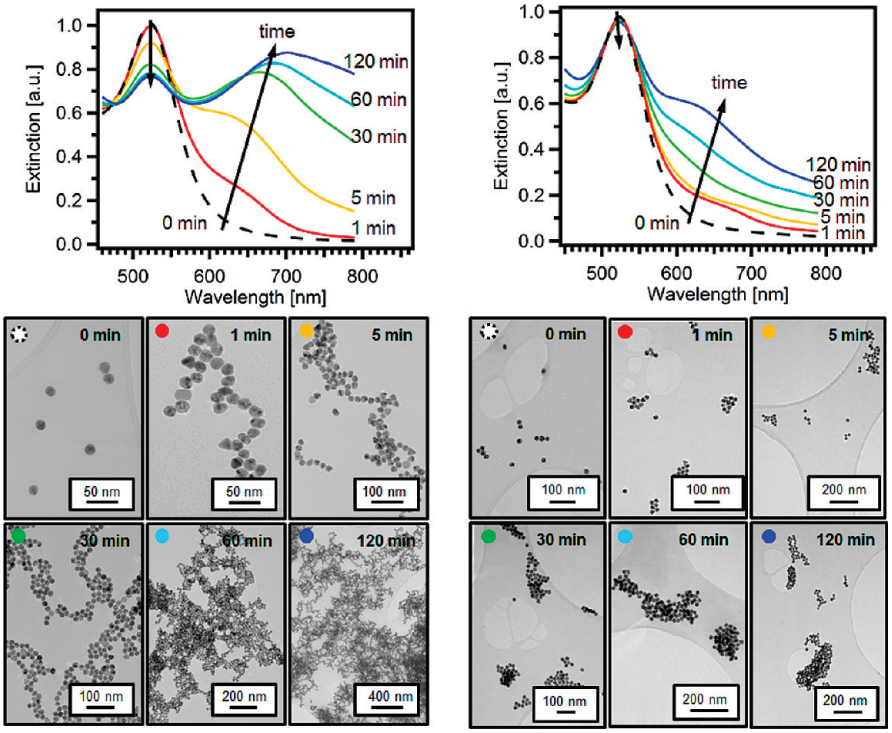

Figure 3. Optical extinction of 1:80 and 1:60 AuNP:CB[5] solutions with increasing time. TEM images from typical aggregation products formed at the indicated time elapsed. Differences in topology correspond to DLCA (left) and RLCA (right) regimes.

the DLCA and RLCA spectra reveals a superposition of two distinct modes centered at 590 and ~650 nm. Fitting to two Lorenztian functions supports this observation and shows that the mode at 590 nm remains stationary in position while the second mode around 650 nm red shifts during aggregation (arrows track the peak). In the case of DLCA, the initial aggregate mode grows rapidly and begins to saturate when the 590 nm mode saturates in intensity (Figure 2e). Subsequently, the resonance at 650 nm then rapidly red shifts, while the mode at 590 nm remains fixed in position. We believe this change in spectral behavior corresponds to a change in the dominant growth mechanism in solution, from the rapid formation of dimers and short chains to the growth of larger size aggregates following the constant DLCA reaction kernel.[43] Time resolving the evolving aggregate through TEM micrographs elucidates the topological origins of the extinction spectra for both kinetic regimes.

Relating Topology with Optical Properties. Insight into the size and topology of the grown AuNP:CB[5] aggregates is provided by TEM images obtained from aliquots extracted from the AuNP:CB[5] 1:80 and 1:60 aggregating solution at different points in time. The samples are dried immediately onto holey carbon grids (Figure 3). By measuring the optical extinction in solution during growth, comparisons can be made between the far-field optics and local aggregate structure.

The TEM of 1:80 AuNP:CB[5] at 1 min reveals the formation of open, elongated chain-like structures. These are consistent with DLCA growth since the colliding particles are unable to reach the very center of growing clusters, instead colliding with higher probability with the outermost structures. Even after 30 min, the clusters remain sparse and open, while after 2 h, quasi-fractal networks on the micrometer-scale form, which is in agreement with the DLCA growth model. A different behavior is apparent for 1:60 AuNP:CB[5] in which tight compact clusters form and slowly grow by RLCA. Throughout, the average particle spacing is ~0.9 nm as determined from analysis of TEM images (Supporting Information Figure S1). This clearly indicates that CB[5] is an effective mediator to bring about aggregation and successfully controls the gap size defined by the molecular geometry (as also shown by the distinct plasmonic modes).

Using these topological insights, we are able to explain the plasmonic evolution within the kinetic models. The subnanometer spacing within the aggregates introduces additional electromagnetic interactions between closely spaced AuNPs, resulting in a shift in their resonance wavelength that increases with the number and proximity of neighboring AuNPs up to a saturation limit.[49−53] The resonance mode at 590 nm is identified as the longitudinal plasmon resonance of a 20 nm particle dimer with a separation of ~1 nm, in close agreement with our theoretical simulations and consistent with the TEM of CB[5]-mediated AuNP aggregates. This mode scales as theoretically expected with AuNP diameter (Figure 2f). After a short time, these dimers are embedded in larger clusters.

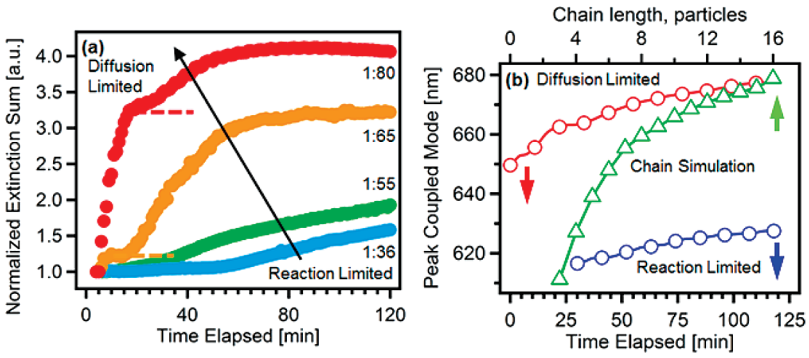

Figure 4. (a) Integrated extinction from 525 to 700 nm (normalized to $t = 0$) for different AuNP:CB[5] ratios (as labeled). (b) Peak wavelength of the fitted coupled mode with time for the DLCA (1:80) and RLCA aggregates (1:55) of Figure 2. Theory for linear chain of NPs also shown using the dielectric function from Johnson and Christy with size correction.[46] Illumination is perpendicular to the axis (field is parallel).

However, our simulations of kinked chains reveal that component dimers may be locally excited within larger disordered chain assemblies. The well-defined "dimer" mode thus arises from *many precisely equivalent CB[5]-defined junctions*. The broader mode at 650 nm is identified as a many-body coupled mode consistent with mutual coupling in the nanochains which progressively undergo resonance shifts with increasing numbers of appropriately illuminated constituent nanoparticles. Theory predicts an inherent saturation in interparticle coupling after ~10 NPs within nanochains, leading to a saturation of the red shift, which is indeed seen experimentally for DLCA aggregates. Surprisingly, our simulations reveal that nonlinear disordered chains support modes similar to those of straight chains (see Supporting Information Figure S2), implying that the model introduced here is robust to structural imperfections. The TEM images show DLCA aggregates to be composed of such chain-like structures, in agreement with the spectral identification of this chain mode. Finally, at long times, the formation of micrometer-sized aggregates at the visible λ scale are seen, and the extinction spectra show a rapidly growing near-infrared tail whose origin is currently poorly understood.[54−57] We identify the mode still remaining near the isolated AuNP resonance at 525 nm as emerging from the transverse mode (with light polarized *across* the chains).

This precisely spaced CB[5]:AuNP system allows far-field interrogation of nanoscale growth with millisecond acquisition times. Existing techniques to probe aggregate growth such as dynamic and static light scattering are only able to reveal an ensemble-average hydrodynamic radius and fractal parameter—a measure of the large-scale aggregate topology over a much longer acquisition time. The data presented here reveal that *in situ* study of local growth is possible, with high sensitivity to nanoscale architecture. In addition to elucidation of local structure, the concentration of CB[5] has a profound effect on the *growth rate and red shift of aggregate plasmon peaks* under both reaction-limited and diffusion-limited aggregation regimes.

Plasmonics of Precise-Spaced Nanoparticle Assemblies. The kinetics of aggregation affects the plasmonic profile of the aggregate through the optically coupled topology. The kinetics may be parametrized from the far-field extinction by monitoring specific wavelengths, but this can be misleading. For example, previous reports have determined the kinetic rate by the *decrease* in the single nanoparticle SPR band[58] (which however is convoluted with the transverse mode of the chains) or by the peak aggregate wavelength[35,59] (which is blurred if the gap separations are not precisely controlled). An improved approach is to measure the integrated extinction over the optically active spectral region from 590 to 700 nm.[33] Here we directly compare the spectral peak shifts in the instantaneous spectra with the integrated extinction, summing the extinction difference spectra from 590 to 700 nm. By increasing the CB[5] to AuNP ratio, the kinetic rates can be varied, altering the dominant topology of the aggregates with direct consequences on their use as SERS substrates. The effect of kinetics on the plasmonics of CB[5]-mediated aggregates is discussed below.

Comparing the integrated extinction as a function of time for various AuNP:CB[5] ratios (Figure 4a) reveals the transition from RLCA to DLCA kinetics with increasing CB[5] concentration. This is consistent with the known growth in hydrodynamic radius, r, with time[44] where the extinction is dominated by the r^6 optical scattering cross section in a quasi-static approach. For the RLCA regime, the low probability of sticking leads to a cluster capture cross section that increases with cluster size, effectively producing an autocatalytic reaction scheme.[60] This is observed as a marked transition in the behavior of the integrated extinction over the lifetime of the aggregation. The RLCA regime shows a linear increase in integrated extinction, while the DLCA displays a sudden change after ~10 min. For the DLCA regimes (1:>60), the aggregation rate appears to be a summation of two mechanisms: the

immediate formation of NP dimers followed by subsequent chain-like multiparticle growth. However, our spectral dynamics reveal this to be a result of the complicated plasmonic origin of these Au nanocomposites. Both the extinction strength and spectral position for clusters increase with number of NPs, but clearly dimers do not disappear from view when they become embedded in larger clusters. Light scattering studies in the past have ignored this complicated optical response: focusing on either single wavelength scattering or integrated extinction is problematic.

Examination of the aggregate mode peak wavelength (Figure 4b) reveals that for the quicker DLCA aggregation much greater red shifts result. We believe that this is due to the longer coupled chain lengths in different directions as compared to the compact RCLA structures (seen in TEMs, Figure 3). By inverting the plasmonic red shifts using the theoretical predictions (Figure 4b), optically accessible chain lengths of ~10 can be inferred, within 20 min growth. In contrast to the open DLCA networks, the compact RLCA clusters show at least 5 times smaller red shifts for similar numbers of NPs in a cluster. We believe the closed RLCA topology effectively shields the embedded nanochain response (unlike embedded dimers), as indicated by our simulations.[61] Hence it is clear that spectral shifts of the longer wavelength plasmonic modes in precisely spaced AuNP clusters give specific information about the nanoscale topology.

SERS from Plasmonic Nanojunctions. As discussed, CB[5] both induces aggregation as well as defines the precise junction separation between two or more AuNPs from its rigid "barrel-shaped" geometry. It is well-known that molecules in such nanogaps between closely coupled nanoparticles experience the most intense field concentration and therefore dominate the SERS spectrum. Since cucurbit[5]urils are Raman-active[5] and the CB[5] cage (which can harbor analyte molecules) is in this most favorable position at the center of a hot spot, and within a nanometer of the Au surface, the AuNP:CB[5] system is a good candidate for a *self-calibrated* SERS substrate. For the 20 nm AuNPs especially employed here, the dimer mode is found at 590 nm and the resonant chain modes at ~650 nm, suitable for resonant excitation by 633 nm light (note the spectral positions can be tuned using different AuNP diameters). The CB[5] molecules thus act as *local reporters* of the optical near-field, and so simultaneous SERS measurements are recorded at different laser excitation wavelengths to understand the effect of resonance matching with the plasmon modes and also to correlate the results with observed far-field extinction. Representative SERS spectra of CB[5] with 633 and 785 nm laser excitation recorded in solution while aggregating 20 nm AuNP are shown in Figure S4 (Supporting Information). The two signature peaks of

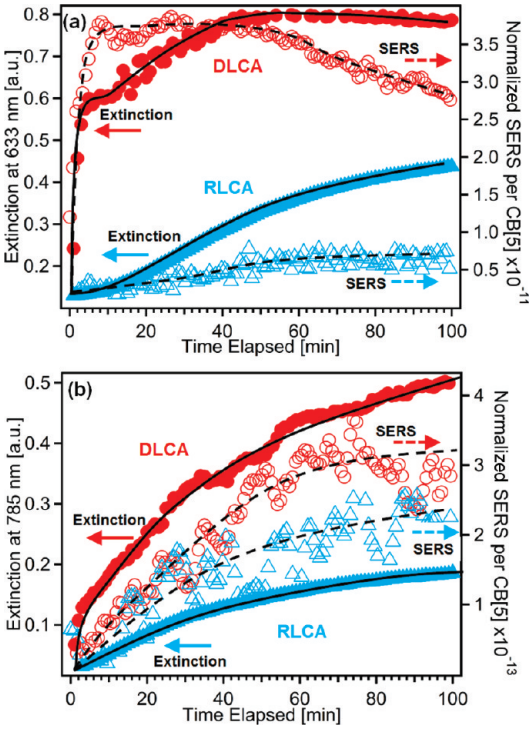

Figure 5. Time-resolved normalized SERS intensity of the 826 cm^{-1} CB[5] Raman mode *vs* time for excitation wavelengths of (a) 633 and (b) 785 nm, correlated with aggregate extinction at the excitation wavelength.

CB[5] at 454 and 826 cm^{-1} are clearly seen with both of these laser wavelengths.

We note that the citrate peaks from the AuNP capping layer are never observed in SERS on monodisperse colloids, clearly suggesting that aggregation and selective molecular placement are required for SERS under these measurement conditions. By measuring the Raman from a known CB[5] solution under similar acquisition conditions, we calculate the bulk (or ensemble-average) enhancement factor (EF) of the AuNP:CB[5] aggregates to be

$$\mathrm{EF} = (I_{\mathrm{SERS}} \times N_{\mathrm{Raman}})/(I_{\mathrm{Raman}} \times N_{\mathrm{SERS}}) = 1 \times 10^{7} \quad (1)$$

where I is the intensity of the signal and N is the number of molecules in the focal volume (concentration × focal volume). The spectra were acquired using the same numerical aperture objective, hence the above expression effectively becomes $(I_{\mathrm{SERS}} \times C_{\mathrm{Raman}})/(I_{\mathrm{Raman}} \times C_{\mathrm{SERS}})$, where C is the concentration of the solution used in the two cases. Since only a small fraction of the CB[5] introduced acts to define the hot spot junctions that contribute to the SERS, the local enhancement factor is expected to be much greater. Based on known fractal dimension estimates for aggregation in the DLCA case,[42−44] we find that less than 0.01% of the initial amount of CB[5] defines the junctions of the aggregates in the focal volume, which gives an enhancement factor of 10^{11}. Thus the Raman enhancement recorded corresponds to the huge field

confinement within the nanopair junctions. In contrast to typical methods of preparing SERS NP aggregates, these SERS enhancements are robust and repeatable.

The plasmon kinetics during aggregation are markedly different for the RLCA and DLCA growth regimes (Figure 2). The SERS enhancements produced by the AuNP:CB[5] aggregate are thus also expected to show sensitivity to growth kinetics. The CB[*n*] molecule acts as a local SERS reporter itself, allowing this to be studied. Thus the SERS signals (at the 826 cm^{-1} peak) from the CB[5]-mediated aggregates are simultaneously acquired (Figure 5) from the solutions studied in Figure 2. The SERS is normalized to counts per milliwatt per CB[5] molecule to allow comparison between the two regimes. Note that not all CB[5] in solution can contribute to the observed SERS. The measured extinction of the aggregates at the different excitation wavelengths is overlaid on the correspondingly induced SERS (Figure 5a,b). The aggregate topology has a clear effect on the SERS, with the DLCA showing more than 10-fold improvement over the RLCA at 633 nm.

Similar to their rapid rise in extinction, the DLCA AuNP:CB[5] aggregates excited at 633 nm (Figure 5a) show immediate strong SERS signals. This arises from resonant matching of maximal plasmonic coupling with the Raman excitation wavelength following dimer and short chain-led aggregation. After 30 min, the extinction saturates but the SERS starts to drop. This difference can be understood from the spectra (Figure 2a) showing the resonant chain mode red-shifting away from the excitation laser, thus moving the aggregate off-resonance. Since the dimer population remains constant in this phase (Figure 2e), this implies that chain modes contribute additionally to the SERS response, and the red-shifting decreases this contribution. The RLCA aggregate, however, reveals a constant increase in extinction following plasmonic coupling which keeps the aggregate band close to the Raman wavelength (Figure 5b). This in turn leads to a steady increase in the SERS.

While the behavior of the SERS strengths and extinction cross sections in Figure 5a,b is clearly related, the SERS is dependent on the fourth power of the *local* field generated at the clusters. This makes quantitative comparison between SERS and extinction less straightforward. The DLCA/RLCA SERS ratio varies as the clustering process evolves at 633 nm (as observed in Figure 5a). However, a systematically larger SERS signal is always obtained for the DLCA compared to RLCA clusters. This is consistent with preliminary model calculations for the near-field in open and compact clusters, respectively. More strikingly, the aggregates show hundred-fold stronger SERS at 633 nm compared to 785 nm. This is a consequence of the nonresonant situation at 785 nm. Despite the significant extinction at these longer wavelengths, the SERS is much weaker.

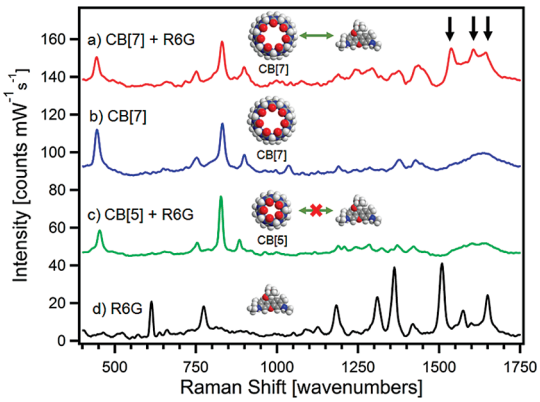

Figure 6. SERS spectra of (a) CB[7] with R6G, (b) CB[7] alone, and (c) CB[5] with R6G are shown. A bulk Raman spectrum of R6G is shown in (d). Single molecules of R6G sequester in the cavity and get exposed to the intense optical fields on binding with CB[7] but not with CB[5]. Signals from R6G (marked by arrows) are clearly visible with CB[7] and absent with CB[5]. The concentrations of CB[*n*] and R6G were ~micromolar and nanomolar, respectively. The spectra are baseline corrected and offset for clarity.

Nevertheless, since the strength of SERS depends on the near-field generated at the clusters, in this nonresonant situation, a lightning rod[62] effect is produced contributing to the weaker but still significant SERS signal. This effect is present for both DLCA and RLCA situations and may be the origin of their similar SERS signals at this longer wavelength. In summary, the CB-reported SERS potential of AuNP:CB[5] aggregate near-fields is shown to be closely related to their easily measured far-field extinction spectra, which also allows SERS to be optimized by simple far-field measurements. The SERS extracted from AuNP:CB[5] aggregate substrates can be finely tuned both temporally and energetically as a function of the CB[5] concentration *via* the growth kinetics, in a completely consistent manner. Thus SERS is an additional sensitive probe of nanoscale architectures in noble-metal NP:CB composites.

Host–Guest SERS. Besides the interesting plasmonic properties arising out of the use of cucurbit[*n*]urils as precise "molecular glue", their host–guest chemistry can be harnessed in sensing applications. Here we employ the host–guest properties of cucurbit[*n*]urils for molecular-recognition-based SERS sensing. We demonstrate this principle with the dye rhodamine 6G (R6G). A slightly larger water-soluble homologue cucurbit[7]uril has been shown to form a strong 1:1 inclusion complex with R6G with a high association constant (>50 000 M^{-1}),[38] whereas the smaller CB[5] cannot accommodate any portion of R6G. Binding to the Au surface through the portal groups,[37] CB[7] can thus be used to capture and expose the guest molecule to the intense optical field when used to aggregate Au nanoparticles. Figure 6a shows the Raman modes of R6G (marked with arrows) inside the AuNP:CB[7] aggregates. Such modes are clearly absent in the case of

AuNP:CB[5] aggregates (Figure 6c), confirming the specificity of cucurbit[*n*]urils for the host–guest binding. For comparison, a bulk Raman spectrum of R6G is shown in Figure 6d. The absence of lower wavenumber Raman modes from R6G is understood to be due to the restriction of specific modes of vibration due to the cavity binding.

This exemplar result shows the potential of this SERS-based selective assay. We have tested our host–guest sensing approach with AuNP:CB[*n*] SERS substrates with other molecules, the results of which will be communicated separately. Nevertheless, it is evident that the wide range of guests for cucurbit[*n*]urils opens up the exciting possibility of multifunctional solution-based selective *self-calibrated* SERS sensors.

CONCLUSION

We have shown that the surface modification of AuNPs by the adsorption of CB[5] molecules produces partially controllable and highly consistent fractal coagulates. Aggregation follows well-known reaction kinetics as a function of CB[5] concentration. Crucially, the aggregates maintain interparticle separations defined by the cucurbit[*n*]uril geometry, regardless of CB[5] concentration. This in turn allows for the consistent formation of distinct plasmon resonances, identified as a NP dimer and coupled NP chain modes.[61] Strong and reproducible SERS is observed from such AuNP:CB[5] aggregates with the cucurbit[*n*]uril molecule itself acting as a SERS reporter, where the exploited resonant plasmon modes can be tuned in spectral position and time through the concentration of CB[5] and the NP diameter. Finally, we demonstrate a SERS-based assay using the host–guest complexation ability of CB[*n*] in which the analyte molecule is subjected to intense field enhancement at the heart of the plasmonic hot spot. This paves the way for widespread use of AuNP:CB[5] aggregates as solution-based self-calibrated SERS substrates in a plethora of selective sensing applications.

EXPERIMENTAL SECTION

CB Synthesis. Synthesis of cucurbit[5]uril was carried out according to the reported procedure by Kim *et al.*[63] Isolation and purification were performed according to methods reported earlier.[37] To observe the effect of the concentration of CB[5] upon the aggregation of the Au nanospheres (diameter 20 nm),[64] an aqueous solution of 2.4 mM CB[5] was made. The solution was diluted 100-fold and 10–20 μL added to 2 mL of the as-supplied AuNPs, initiating aggregation. The initial AuNP:CB[5] solution was stirred gently for *ca.* 10 s with a magnetic bar to aid thorough mixing. Inspection of the AuNP:CB[5] solution revealed a color change from ruby red to purple, indicative of the coagulation of Au colloids.

Extinction Measurements. A polystyrene cuvette, path length 10 mm, was used to contain the AuNP:CB[5] solution while illuminating with a focused 400–1000 nm tungsten halogen light source (Ocean Optics, LS-1). The transmitted light was collected and sampled with a TE-cooled spectrometer (Ocean Optics, QE 65000) using custom-written software allowing for time-resolved spectroscopy.

Electron Microscopy. Transmission electron microscopy (TEM) was carried out on a JEOL 2000FX TEM under an accelerating voltage of 200 kV. Samples were prepared by applying one drop of the reaction mixture containing AuNP:CB[5] at different elapsed times onto a holey carbon coated copper TEM grid (400 mesh).

SERS Measurements. SERS measurements were performed on a Renishaw InVia Raman confocal microscope with a 5× (NA = 0.12) objective in the backscattering geometry. The spectral acquisition time was 10 s with a 1200 lines mm^{-1} grating, giving a resolution of 4 cm^{-1}. The solution was excited with the 633 and 785 nm laser lines from HeNe and solid-state lasers, respectively. All measurements were performed at room temperature and were calibrated with respect to Si. Both the time-resolved Raman and extinction measurements were performed simultaneously on each aggregating solution.

Acknowledgment. This work was supported by EPSRC EP/F059396/1, EP/G060649/1, EP/H007024/1, EP/H028757/1, and EU NanoSci-E+ CUBiHOLE grants.

Supporting Information Available: Interparticle size distribution from TEM analysis along with additional simulation data for kinked and linear AuNP chains is provided. This material is available free of charge *via* the Internet at http://pubs.acs.org.

REFERENCES AND NOTES

1. Fleischmann, M.; Hendra, P. J.; McQuillan, A. J. Raman Spectra of Pyridine Adsorbed at a Silver Electrode. *Chem. Phys. Lett.* **1974,** *26*, 163–166.
2. Moskovits, M. Surface-Enhanced Spectroscopy. *Rev. Mod. Phys.* **1985,** *57*, 783–826.
3. Albrecht, M. G.; Creighton, J. A. Anomalously Intense Raman Spectra of Pyridine at a Silver Electrode. *J. Am. Chem. Soc.* **1977,** *99*, 5215–5217.
4. Jeanmaire, D. L.; Van Duyne, R. P. Surface Raman Spectroelectrochemistry: Part I. Heterocyclic, Aromatic, and Aliphatic Amines Adsorbed on the Anodized Silver Electrode. *J. Electroanal. Chem.* **1977,** *84*, 1–20.
5. Mahajan, S.; Lee, T.-C.; Biedermann, F.; Hugall, J. T.; Baumberg, J. J.; Scherman, O. A. Raman and SERS Spectroscopy of Cucurbit[*n*]urils. *Phys. Chem. Chem. Phys.* **2010,** *12*, 10429–10433.
6. Lal, S.; Grady, N. K.; Kundu, J.; Levin, C. S.; Lassiter, J. B.; Halas, N. J. Tailoring Plasmonic Substrates for Surface Enhanced Spectroscopies. *Chem. Soc. Rev.* **2008,** *37*, 898–911.
7. Graham, D. The Next Generation of Advanced Spectroscopy: Surface Enhanced Raman Scattering from Metal Nanoparticles. *Angew. Chem., Int. Ed.* **2010,** *49*, 9235–9237.
8. Schwartzberg, A. M.; Grant, C. D.; Wolcott, A.; Talley, C. E.; Huser, T. R.; Bogomolni, R.; Zhang, J. Z. Unique Gold Nanoparticle Aggregates as a Surface-Enhanced Raman Scattering Substrate. *J. Phys. Chem. B* **2004,** *108*, 19191–19197.
9. Hao, E.; Schatz, G. C. Electromagnetic Fields around Silver Nanoparticles and Dimers. *J. Chem. Phys.* **2004,** *120*, 357–366.
10. Kneipp, K.; Wang, Y.; Kneipp, H.; Perelman, L. T.; Itzkan, I.; Dasari, R. R.; Feld, M. S. Single Molecule Detection Using Surface-Enhanced Raman Scattering (SERS). *Phys. Rev. Lett.* **1997,** *78*, 1667–1670.
11. Sztainbuch, I. W. The Effects of Au Aggregate Morphology on Surface-Enhanced Raman Scattering Enhancement. *J. Chem. Phys.* **2006,** *125*, 124707–124712.
12. Le Ru, E. C.; Etchegoin, P. G. Sub-wavelength Localization of Hot-Spots in SERS. *Chem. Phys. Lett.* **2004,** *396*, 393–397.
13. Rodriguez-Lorenzo, L.; Alvarez-Puebla, R. A.; Pastoriza-Santos, I.; Mazzucco, S.; Stephan, O.; Kociak, M.; Liz-Marzan,

L. M.; Garcia de Abajo, F. J. Zeptomol Detection through Controlled Ultrasensitive Surface-Enhanced Raman Scattering. *J. Am. Chem. Soc.* **2009,** *131*, 4616–4618.
14. Lim, D.-K.; Jeon, K.-S.; Kim, H. M.; Nam, J.-M.; Suh, Y.-D. Nanogap-Engineerable Raman-Active Nanodumbbells for Single-Molecule Detection. *Nat. Mater.* **2010,** *9*, 60–67.
15. Nie, S.; Emory, S. R. Probing Single Molecules and Single Nanoparticles by Surface-Enhanced Raman Scattering. *Science* **1997,** *275*, 1102–1106.
16. Xu, H.; Bjerneld, E. J.; Kall, M.; Borjesson, L. Spectroscopy of Single Hemoglobin Molecules by Surface Enhanced Raman Scattering. *Phys. Rev. Lett.* **1999,** 4357–4360.
17. Xu, H.; Aizpurua, J.; Kall, M.; Apell, P. Electromagnetic Contributions to Single-Molecule Sensitivity in Surface-Enhanced Raman Scattering. *Phys. Rev. E* **2000,** *62*, 4318–4324.
18. Wustholz, K. L.; Henry, A.-L.; McMahon, J. M.; Freeman, R. G.; Valley, N.; Piotti, M. E.; Natan, M. J.; Schatz, G. C.; Van Duyne, R. P. Structure−Activity Relationships in Gold Nanoparticle Dimers and Trimers for Surface-Enhanced Raman Spectroscopy. *J. Am. Chem. Soc.* **2010,** *132*, 10903–10910.
19. Myers, D. *Surfaces, Interfaces and Colloids*; Wiley-VCH: New York, 1999; Chapters 4, 5, and 10.
20. Creighton, J. A. In *Surface Enhanced Raman Scattering*; Chang, R. K., Furtak, T. E., Eds.; Plenum: New York, 1982; p 315.
21. Meakin, P. In *The Fractal Approach to Heterogeneous Chemistry*; Avnir, D., Ed.; Wiley: New York, 1989; p 131.
22. Weitz, D. A.; Oliveria, M. Fractal Structures Formed by Kinetic Aggregation of Aqueous Gold Colloids. *Phys. Rev. Lett.* **1984,** *52*, 1433–1436.
23. Girard, C.; Dujardin, E.; Li, M.; Mann, S. Theoretical Near-Field Optical Properties of Branched Plasmonic Nanoparticle Networks. *Phys. Rev. Lett.* **2006,** *97*, 100801.
24. De Waele, E.; Koenderink, A. F.; Polman, A. Tunable Nanoscale Localization of Energy on Plasmon Particle Arrays. *Nano Lett.* **2007,** *7*, 2004–2008.
25. Harris, N.; Arnold, M. D.; Blaber, M. G.; Ford, M. J. Plasmonic Resonances of Closely Coupled Gold Nanosphere Chains. *J. Phys. Chem. C* **2009,** *113*, 2784–2791.
26. Matsushita, M. In *The Fractal Approach to Heterogeneous Chemistry*, Avnir, D., Ed.; Wiley: New York, 1989; p 161.
27. Li, W.; Camargo, P. H. C.; Lu, X.; Xia, Y. Dimers of Silver Nanospheres: Facile Synthesis and Their Use as Hot Spots for Surface-Enhanced Raman Scattering. *Nano Lett.* **2009,** *9*, 485–490.
28. Jarvis, R. M.; Rowe, W.; Yaffe, N. R.; O'Conner, R.; Knowles, J. D.; Blanch, E. W.; Goodacre, R. Multiobjective Evolutionary Optimisation for Surface-Enhanced Raman Scattering. *Anal. Bioanal. Chem.* **2010,** *397*, 1893–1901.
29. Novotny, L; Hecht, B. *Principles of Nano-Optics*; Cambridge University Press: Cambridge, UK, 2006; pp 378−419.
30. Bernard, L.; Kamdzhilov, Y.; Calame, M.; Jan van der Molen, S.; Liao, J.; Schonenberger, C. J. Spectroscopy of Molecular Junction Networks Obtained by Place Exchange in 2D Nanoparticle Arrays. *J. Phys. Chem. C* **2007,** *111*, 18445–18450.
31. Park, S. Y.; Lee, J.-S.; Georganopoulou, D.; Mirkin, C. A.; Schatz, G. C. Structures of DNA-Linked Nanoparticle Aggregates. *J. Phys. Chem. B* **2006,** *110*, 12673–12681.
32. Li, M.; Wong, K. K. W.; Mann, S. Organization of Inorganic Nanoparticles Using Biotin-Streptavidin Connectors. *Chem. Mater.* **1999,** *11*, 23–26.
33. Aslan, K.; Luhrs, C. C.; Perez-Luna, V. H. Controlled and Reversible Aggregation of Biotinylated Gold Nanoparticles with Streptavidin. *J. Phys. Chem. B* **2004,** *108*, 15631–15639.
34. Feldheim, D. Assembly of Metal Nanoparticle Arrays Using Molecular Bridges. *Electrochem. Soc. Interface* **2001,** 22–25.
35. Dammer, O.; Vlckova, B.; Prochazka, M.; Sedlacek, J.; Vohlidal, J.; Pfleger, J. Morphology and Optical Responses of SERS Active π-Conjugated Poly(*N*-ethyl-2-ethynylpyridinium iodide)/Ag Nanocomposite Systems. *Phys. Chem. Chem. Phys* **2009,** *11*, 5455–5461.
36. An, Q.; Guangtao, L.; Tao, C.; Li, Y.; Wu, Y.; Zhang, W. A General and Efficient Method To Form Self-Assembled Cucurbit[*n*]uril Monolayers on Gold Surfaces. *Chem. Commun.* **2008,** 1989–1991.
37. Lee, T.-C.; Scherman, O. A. Formation of Dynamic Aggregates in Water by Cucurbit[5]uril Capped with Gold Nanoparticles. *Chem. Commun.* **2010,** *46*, 2438–2440.
38. Mohanty, J.; Nau, W. M. Ultrastable Rhodamine with Cucurbituril. *Angew. Chem.* **2005,** *117*, 3816–3820.
39. Lagona, J.; Mukhopadhyay, P.; Chakrabarti, S.; Isaacs, L. The Cucurbit[*n*]uril Family. *Angew. Chem., Int. Ed.* **2005,** *44*, 4844–4870.
40. Marquez, C.; Huang, F.; Nau, W. M. Cucurbiturils: Molecular Nanocapsules for Time-Resolved Fluorescence-Based Assays. *IEEE Trans. Nanobiosci.* **2004,** *3*, 39–45.
41. Lin, M. Y.; Lindsay, H. M.; Weitz, D. A.; Ball, R. C.; Klein, R.; Meakin, P. Universality in Colloid Aggregation. *Nature* **1989,** *339*, 360–362.
42. Lin, M. Y.; Lindsay, H. M.; Weitz, D. A.; Ball, R. C.; Klein, R.; Meakin, P. Universal Reaction-Limited Colloid Aggregation. *Phys. Rev. A* **1990,** *41*, 2005–2010.
43. Lin, M. Y.; Lindsay, H. M.; Weitz, D. A.; Klein, R.; Ball, R. C.; Meakin, P. Universal Diffusion-Limited Aggregation. *J. Phys.: Condens. Matter* **1990,** *2*, 3093–3113.
44. Meakin, P. Aggregation Kinetics. *Phys. Scr.* **1992,** *46*, 295–331.
45. García de Abajo, F. J.; Howie, A. Retarded Field Calculation of Electron Energy Loss in Inhomogeneous Dielectrics. *Phys. Rev. B* **2002,** *65*, 115418.
46. Johnson, P. B.; Christy, R. W. Optical Constants of the Noble Metals. *Phys. Rev. B* **1972,** *6*, 4370–4379.
47. Maier, A. M. *Plasmonics Fundamentals and Applications*; Springer: New York, 2007; p 162.
48. Bohren, C. F.; Huffman, D. R. *Absorption and Scattering of Light by Small Particles*; Wiley-Interscience: New York, 1983; pp 75−80.
49. Kreibig, U.; Vollmer, M. In *Optical Properties of Metal Clusters*; Toennies, J. P., Ed.; Springer: Berlin, 1995; p 23.
50. Myroshnychenko, V.; Rodríguez-Fernandez, J.; Pastoriza-Santos, I.; Funston, A. M.; Novo, C.; Mulvaney, P.; Liz-Marzan, L. M.; García de Abajo, F. J. Modelling the Optical Response of Gold Nanoparticles. *Chem. Soc. Rev.* **2008,** *37*, 1792–1805.
51. Ghosh, S. K.; Pal, T. Interparticle Coupling Effect on the Surface Plasmon Resonance of Gold Nanoparticles: From Theory to Applications. *Chem. Rev.* **2007,** *107*, 4797–4862.
52. Daniel, M.-C.; Astruc, D. Gold Nanoparticles: Assembly, Supramolecular Chemistry, Quantum-Size-Related Properties, and Applications toward Biology, Catalysis, and Nanotechnology. *Chem. Rev.* **2004,** *104*, 293–346.
53. Alu, A.; Engheta, N. Theory of Linear Chains of Metamaterial/Plasmonic Particles as Subdiffraction Optical Nanotransmission Lines. *Phys. Rev. B* **2006,** *74*, 2054361–18.
54. Klar, T. A. Biosensing with Plasmonic Nanoparticles. In *Nanophotonics with Surface Plasmons*; Shalaev, V. M., Kawata, S., Eds.; Elsevier: Amsterdam, 2007; pp 253−256.
55. Quinten, M. Optical Effects Associated with Aggregates of Clusters. *J. Clust. Sci.* **1999,** *10*, 319–358.
56. Norman, T. J.; Grant, C. D.; Magana, D.; Zhang, J. Z.; Liu, J.; Cao, D.; Bridges, F.; Van Buuren, A. Near Infrared Optical Absorption of Gold Nanoparticle Aggregates. *J. Phys. Chem. B* **2002,** *106*, 7005–7012.
57. Liebsch, A.; Persson, B. N. J. Optical Properties of Small Metallic Particles in a Continuous Dielectric Medium. *J. Phys. C: Solid State* **1983,** *16*, 5375–5391.
58. Moskovits, M.; Vlckova, B. Adsorbate-Induced Silver Nanoparticle Aggregation Kinetics. *J. Phys. Chem. B* **2005,** *109*, 14755–14758.
59. Aslan, K.; Lakowicz, J. R.; Geddes, C. D. Nanogold Plasmon Resonance-Based Glucose Sensing. 2. Wavelength-Ratiometric Resonance Light Scattering. *Anal. Chem.* **2005,** *77*, 2007–2014.
60. Lynch, N. J.; Kilpatrick, P. K.; Carbonell, R. G. Aggregation of Ligand-Modified Liposomes by Specific Interactions with Proteins. I: Biotinylated Liposomes and Avidin. *Biotechnol. Bioeng.* **1996,** *50*, 151–168.

61. To be communicated in a subsequent publication.
62. Le, F.; Brandl, D. W.; Urzhumov, Y. A.; Wang, H.; Kundu, J.; Halas, N. J.; Aizpurua, J.; Nordlander, P. Metallic Nanoparticle Arrays: A Common Substrate for Both Surface-Enhanced Raman Scattering and Surface-Enhanced Infrared Absorption. *ACS Nano* **2008,** *2*, 707–718.
63. Kim, J.; Jung, I.-S.; Kim, S.-Y.; Lee, E.; Kang, J.-K.; Sakamoto, S.; Yamaguchi, K.; Kim, K. New Cucurbituril Homologues: Syntheses, Isolation, Characterization, and X-ray Crystal Structures of Cucurbit[*n*]uril (*n* = 5, 7, and 8). *J. Am. Chem. Soc.* **2000,** *122*, 540–541.
64. EM.GC20, British Biocell International.